J. Fluid Mech. (1997), *vol.* 335, *pp.* 1–28

The wall jet in a rotating fluid

By MELVIN E. STERN[1], ERIC P. CHASSIGNET[2]
AND J. A. WHITEHEAD[3]

[1] Department of Oceanography, Florida State University, Tallahassee, FL 32306-3048, USA
e-mail: stern@ocean.fsu.edu
[2] RSMAS/MPO, University of Miami, Coral Gables, FL 33124, USA
e-mail: echassignet@rsmas.miami.edu
[3] Woods Hole Oceanographic Institution, MA 02543, USA
e-mail: jwhitehead@whoi.edu

(Received 10 March 1996 and in revised form 24 September 1996)

The previously observed spatial evolution of the two-dimensional turbulent flow from a source on the vertical wall of a shallow layer of rapidly rotating fluid is strikingly different from the non-rotating three-dimensional counterpart, insofar as the instability eddies generated in the former case cause the flow to separate completely from the wall at a finite downstream distance. In seeking an explanation of this, we first compute the temporal evolution of two-dimensional finite-amplitude waves on an unstable laminar jet using a finite difference calculation at large Reynolds number. This yields a dipolar vorticity pattern which propagates normal to the wall, while leaving some of the near-wall vorticity (negative) of the basic flow behind. The residual far-field eddy therefore contains a net positive circulation and this property is incorporated in a heuristic point-vortex model of the spatial evolution of the instability eddies observed in a laboratory experiment of a flow emerging from a source on a vertical wall in a rotating tank. The model parameterizes the effect of Ekman bottom friction in decreasing the circulation of eddies which are periodically emitted from the source flow on the wall. Further downstream, the point vortices of the model merge and separate abruptly from the wall; the statistics suggest that the downstream separation distance scales with the Ekman spin-up time (inversely proportional to the square root of the Coriolis parameter f) and with the mean source velocity. When the latter is small and f is large, qualitative support is obtained from laboratory experiments.

1. Introduction

An unsolved problem in the dynamics of boundary currents is the parameterization of the effect of eddies on the mean flow. In the case of a non-rotating high-Reynolds-number barotropic wall jet emerging from a source on a wall, the three-dimensional turbulence produces a self-similar mean velocity profile spreading continuously downstream along the wall at a small angle (Wygnanski, Katz & Horev 1992). A vastly different behaviour occurs in the rotating version of this problem as the three-dimensional turbulence is suppressed, and barotropic vorticity conservation in a shallow fluid layer produces two-dimensional eddies. This was also observed in laboratory experiments (Stern & Whitehead 1990) in which a wall jet (figure 1*a*) was produced by the flux from a capillary nozzle placed at mid-depth along a vertical wall in a large rotating tank. Although the flow emerging from the capillary nozzle is three-dimensionally turbulent (with entrainment), the Taylor–Proudman effect of rotation

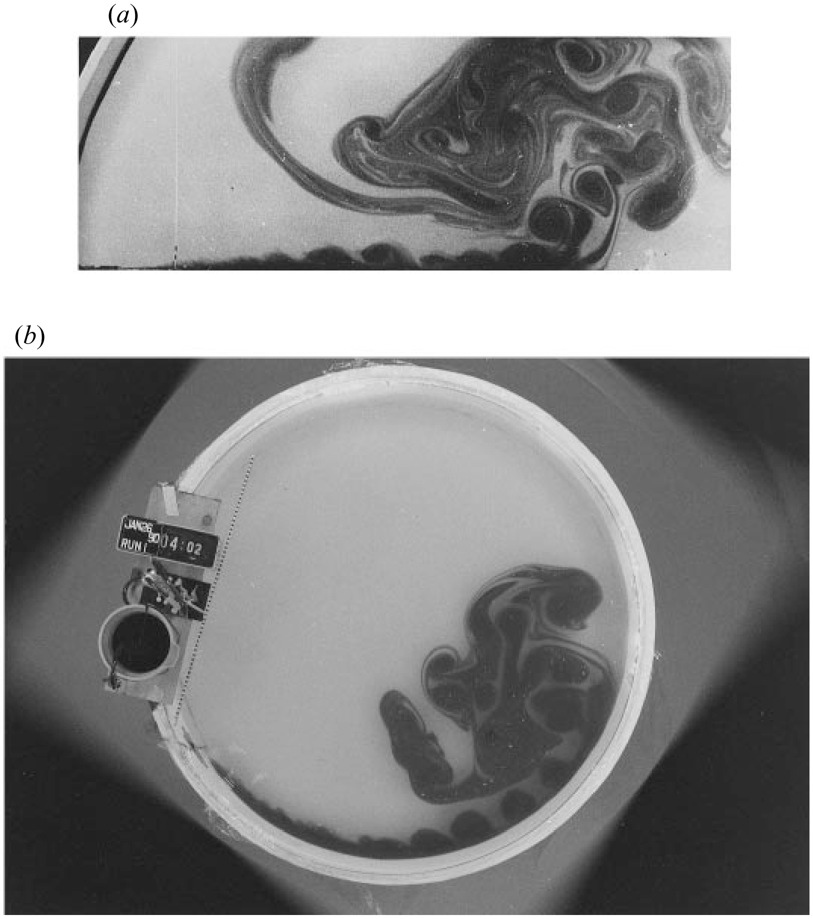

FIGURE 1. Separation of a dyed wall jet issuing from a capillary nozzle in a rotating tank of water. (*a*) After Sten & Whitehead (1990). The vertical wall lies along a diameter (213 cm). Depth of fluid $= 20$ cm. Flow rate $= 5.7\ \mathrm{cm^3\ s^{-1}}$. Time $= 5$ min. after start of flow. (*b*) The flow is now along the circular outer wall of the tank, water depth $= 20$ cm, rotation period $= 15.2$ s, discharge $= 760\ \mathrm{cm^3\ min^{-1}}$. The instability eddies are visible upstream from the point where the jet separates from the wall.

appears further downstream, and the eddies that then appear evolve from two-dimensional instabilities of the barotropic wall jet. The novel and noteworthy effect here, when compared to the non-rotating case (Wygnanski *et al.* 1992), is the rapid deceleration of the dyed nose of the wall current and its apparent stagnation, at which point the eddies detach from the wall and interact in a two-dimensional turbulent plume extending normal to the wall. In figure 1(*a*) the wall flow lies along a diameter of the rotating tank where the small variation of the free-surface height introduces a dynamical 'β-effect'; this was virtually eliminated in a follow-up experiment (figure 1*b*) where the flow was directed along the circular outer wall of the tank, whose radius of curvature is so large compared to the upstream jet width that the wall curvature may be neglected. We can clearly see the instability waves in the upstream jet evolving into round eddies separated by (clear) entrained exterior fluid. Further downstream, these eddies decelerate, merge, separate from the wall and interact with each other in the two-dimensional turbulent plume. Essentially all of the upstream jet leaves the wall before the separation point, as revealed by small white paper pellets strewn into the current.

In this paper, the various mechanisms involved in the separation process of the two-dimensional barotropic wall jet are examined by a combination of numerical and analytical methods as well as laboratory experiments In §2, the eddies appearing in the barotropic jet upstream of the separation point are discussed in terms of the finite-amplitude growth of a periodic disturbance in a uniform downstream current. The qualitative agreement observed between the numerical solutions and some features of the laboratory experiments is then used in §3.1 in an attempt to explain the abrupt separation of the jet from the boundary. Accordingly, the results from §2 are incorporated into a model in which discrete vortices are emitted from a source near a wall, then interact and decay as they move downstream; eventually, each point vortex is ejected from the wall into a large plume, and the statistics of this ensemble provides a basis for the experimental investigation (§3.2) of the separation point. The different physical effects are then summarized and discussed in the concluding section along with suggestions for future work.

2. Finite-amplitude instability in the two-dimensional wall jet

In this section, we consider the finite-amplitude shear instabilities in a downstream-uniform wall jet. Etling, Hansen & Jürrens (1993) have investigated this experimentally and numerically for a jet on an inner circular wall of relatively small radius in a rotating tank. Their initial wall jet was produced by first increasing the inner-wall angular velocity (relative to the outer wall) and then decreasing it. The generated current then develops a normal-mode instability, in which the positive- and negative-vorticity layers evolve into individual cores which form an azimuthally periodic array of dipolar ('mushroom-like') eddies, each of which contains two vortices with oppositely circulating streamlines. Because of the divergent radial geometry each dipole tends to propagate independently and monotonically radially outwards from the wall until it dissipates by viscosity. A quite different secular evolution occurs for a jet on a straight wall, in which case adjacent dipoles do not separate but interact with each other.

Calculations of the nonlinear inviscid instability of a piecewise-uniform-vorticity wall jet were made by Bidlot & Stern (1994), but they were limited to a relatively short time interval because of the uncertainties on how to perform the contour dynamical surgery with the required accuracy. In §2.1, finite-difference calculations are therefore performed to examine the behaviour over longer time. It is shown that, in the fully developed instability, the positive and negative vortices eventually change partners (nearest neighbours), thereby reversing the outward movement from the wall, and producing a counter-gradient momentum flux. A point-vortex model is then presented in §2.2 to explain some of the properties of the fully developed timewise instability. Since the question of the role of subharmonic instabilities is also of interest, some results for this case are presented in §2.3. Finally, we remind the reader that in a two-dimensional rotating barotropic flow, the Coriolis force is parametrically irrelevant as its curl vanishes. The following results therefore apply to both rotating and non-rotating cases.

2.1. *Evolution of the wall jet using finite-difference numerical simulations*

Figure 2 (after Bidlot & Stern 1994) shows the evolution of the most unstable normal mode (of wavelength $\lambda = 4.87$) on an undisturbed laminar jet with a triangular profile symmetric about $y = 1$ and with maximum velocity of unity. Two curvilinear material

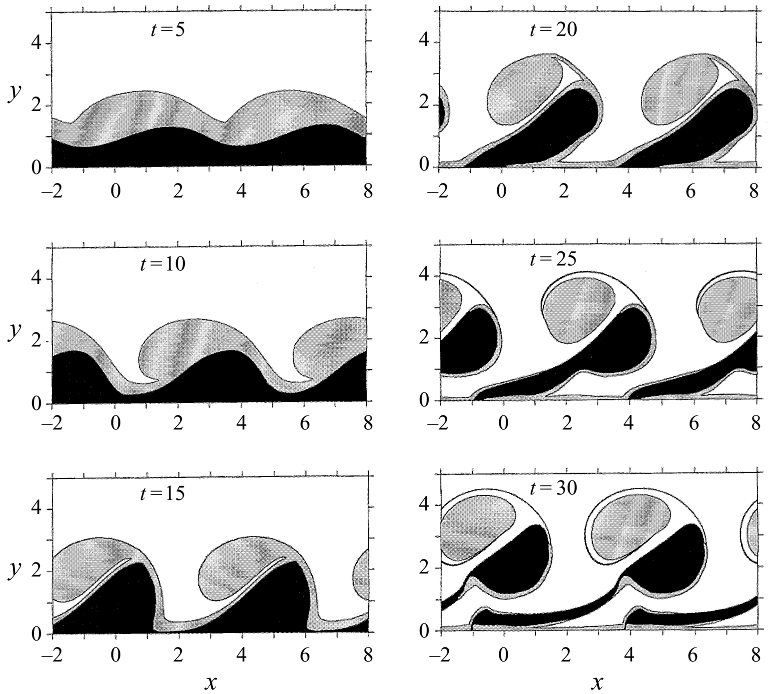

FIGURE 2. The nonlinear inviscid evolution of an unstable piecewise-uniform-vorticity wall jet with unit maximum undisturbed velocity at $y = w = 1$. The displacements of the vorticity interfaces were computed by contour dynamics from $t = 5$ to $t = 30$ (after Bidlot & Stern 1994). Note the negative (darker) vorticity left behind ($t = 30$) on the wall as the dipole propagates away.

interfaces bound the outer layer of uniform positive (counterclockwise) vorticity, and the $y = 0$ wall bounds the darker shaded negative (vorticity) layer. The initial linear growth phase ($t = 5$) is followed by the displacement towards the wall of irrotational fluid (unshaded) and by the formation (at $t = 30$) of fully developed dipolar vortices. Note that as these propagate away from the wall, some of the negative vorticity is left behind, resulting in a dipole which possesses a net positive circulation. If the outward propagating tendency were to continue beyond $t = 30$, the result would resemble the monotonic outward displacement (with eventual decay) observed by Etling *et al.* (1993). Such a tendency, however, is highly unlikely in our case because the unbalanced (net excess positive vorticity) dipole would tend to rotate in a large-diameter circle, so that negative vorticity would eventually appear at larger distances from the wall than positive vorticity, and this negative vorticity implies an unrealistic reversed mean horizontal velocity. We shall show in the following numerical experiments that such a monotonic outward propagation does not occur in the periodic rectilinear geometry because the distance between two successive dipole pairs remains constant. In the circular geometry of Etling *et al.* (1993) the azimuthal distance between radially propagating dipole pairs increases, so that they do not interact strongly.

The finite-difference code of Bleck & Boudra (1986) was used to obtain two-dimensional solutions of the Navier–Stokes equations at high Reynolds number for the same undisturbed flow ($t = 0$ in figure 2) and the same perturbation wavelength λ, but for longer times. Either a no-slip boundary condition (as realized experimentally) or a free-slip condition was imposed on the wall. (One reason for including the latter condition is that it provides some connection and comparison with the inviscid

Experiment	A	Boundary condition	Integration time T
E0	0	Free-slip	100
E1	5×10^{-4}	Free-slip	200
E2	1×10^{-3}	Free-slip	100
E3	5×10^{-4}	No-slip	100

TABLE 1. Parameters of the numerical experiment. Free-slip ($\partial u/\partial y = 0$; $v = 0$) at the wall. No-slip: ($u = 0$; $v = 0$) at the wall.

calculation of Bidlot & Stern (1994); also the free-slip boundary condition is commonly used in oceanographic modelling studies (Haidvogel, McWilliams & Gent 1992).) In addition to the rigid wall at $y = 0$, the numerics require another rigid boundary at some distant y. Calculations for two different Reynolds numbers ($1/A$) were made in a cyclic square domain containing 200×201 grid points separated by the non-dimensional distance $d = 0.0487$. The non-dimensionalization is based on an undisturbed jet with a maximum velocity $u = 1$ at $y = 1$, decreasing linearly to $u = 0$ at $y = 0$ and at $y = 2$. The time step is 0.02; table 1 lists the total integration time, the non-dimensional viscosity (A), and the viscous boundary condition for the different runs.

In addition, passive tracers are also used to diagnose the evolution of the initially piecewise-uniform vorticity distribution. The initial tracer concentration is 1000 in the negative-vorticity band, 500 in the positive-vorticity band and 0 at $y > 2$. The numerical advection was performed with the Flux Corrected Transport (FCT) algorithm (Boris & Book 1973; Zalesak 1979) which combines the smoothness properties of the positive-definite upstream differencing scheme with the accuracy of space-centred schemes, and controls the tendency to generate negative tracer concentration when solving the tracer equation. A small diffusion coefficient (5×10^{-5}) is applied to the Fickian tracer equation.

Although all experiments are started with a small disturbance of wavelength equal to the value for maximum growth on an initial piecewise-uniform mean vorticity flow, the imposed initial perturbation was not the inviscid normal mode used in Bidlot & Stern (1994), but consisted of a small transverse velocity $v_0 = \alpha y \cos(2\pi x/4.87)$ with $\alpha = 0.025$ for $y < 2$ and $\alpha = 0.05$ for $y > 2$. For $A = 0$, this perturbation (not shown) evolved into an approximate normal mode after the short time interval of $t = 5$, as was verified in run E0 (table 1) by measuring the downstream phase shift between vorticity isopleths at different y-levels. Although the wave amplitude at this time was much larger than initially, there is not much harmonic (nonlinear) distortion, and the downstream phase shift (not shown) is in very good agreement with the linear modes of Bidlot & Stern (1994). Furthermore, dipolar vortices similar to the ones in figure 2 were observed to form later, although they were accompanied by considerable numerical noise (since $A = 0$). The noise level is reduced in the more relevant viscous runs E1, E2 and E3 (table 1). Although the diffusion of the initial vorticity discontinuities for these cases precludes quantitative comparisons of phase shift with the theory of Bidlot & Stern (1994), estimates made at $t = 10$ were consistent with those obtained for $A = 0$. In the remainder of this section, vorticity (figures 3, 5 and 7) and tracer distribution (figures 4, 6 and 8) are displayed and discussed at several characteristic times.

We first concentrate on the free-slip experiments E1 and E2 and then compare their evolution with the experimentally realizable no-slip counterpart E3. In both E1 and E2,

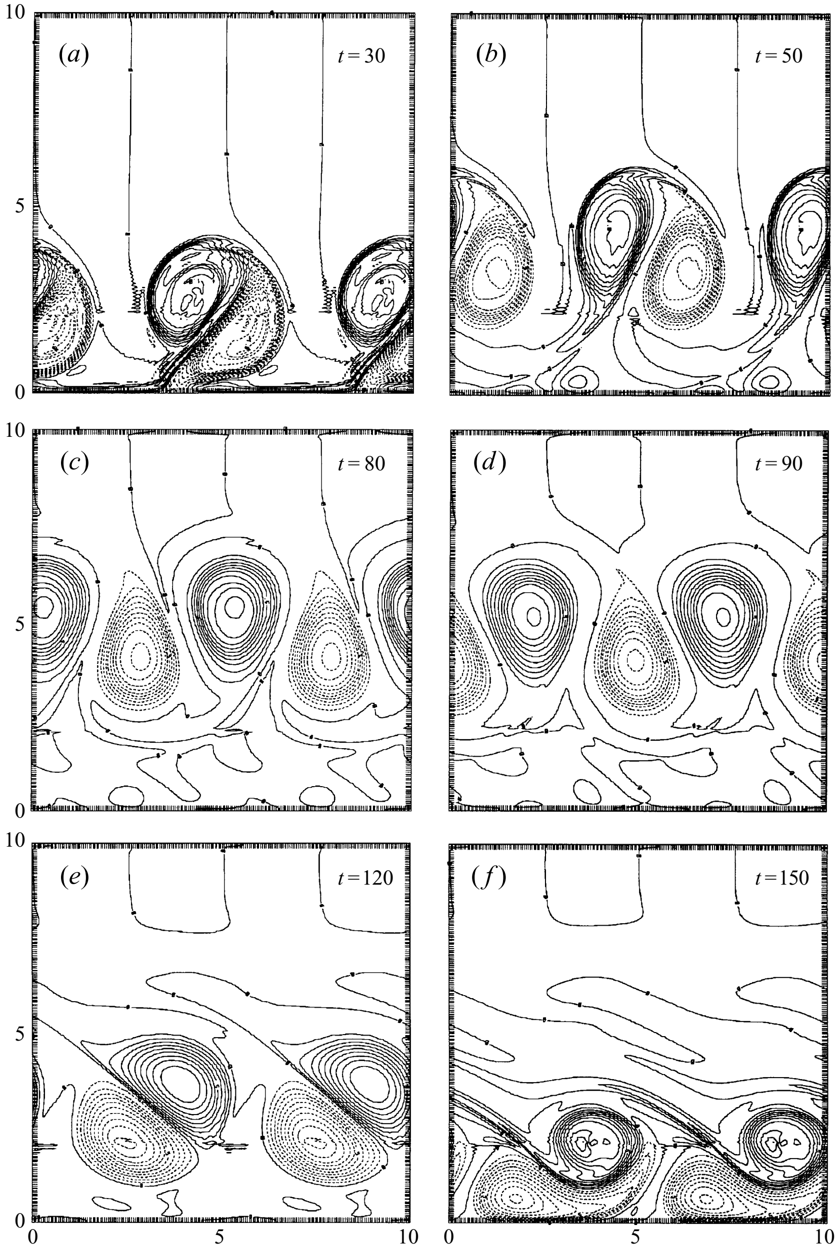

FIGURE 3(*a*–*f*). For caption see facing page.

the unstable waves evolve at $t = 30$ (figures 3*a*, 4*a*, 5*a*, 6*a*) into fully developed vorticity dipoles similar to the inviscid model (figure 2) at these times. The inclination of the dipole axis (like the tilt of the phase lines in the normal mode) is such as to transport momentum to larger y (cf. the mean profiles and the later discussion). As time increases, the slope of the dipole axis in E1 (cf. figures 3*b*, *c*, 4*b*, *c*) changes and the separation between the centroids of neighbouring positive and negative members increases; likewise for the larger-viscosity run E2 (figures 5*b*, *c*, 6*b*, *c*). Thus the phase locking (of the linear growth stage) between the vortices in each dipole is broken in the

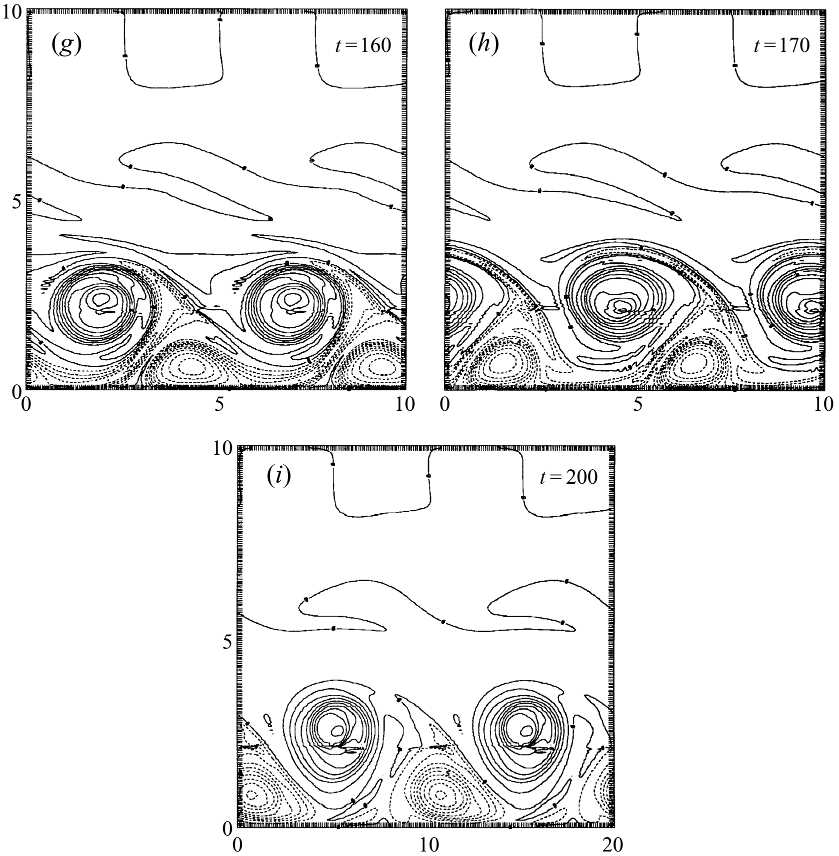

FIGURE 3. Vorticity fields for run E1 (free-slip boundary conditions, $A = 5\times10^{-4}$) at different representative times of the numerical integration. The contour interval is 0.1. The undisturbed triangular jet and the fundamental wavelength ($\lambda = 4.87$) are the same as in figure 2. Note that the negative vortices move downstream faster than the positive ones.

latter stage of dipole development, and the negative members move downstream more rapidly. Eventually, there is a change of 'partners' (nearest neighbour) and a reversal of the slope of the axis of the new dipoles as seen in figures 3(*d*, *e*), 4(*d*, *e*) for E1 and figures 5(*d*, *e*), 6(*d*, *e*) for E2. It is visually apparent from figure 5(*d*) that the magnitude of the integrated negative vorticity in the dipole is less than the integrated positive vorticity, and this important property is discussed below in detail. The slope reversal of the dipole axis is also accompanied by a reversal of the outward movement of the eddies (cf. figures 3*d*, *e*, *f* for E1 and 5*d*, *e* for E2). Another important effect is the entrainment of the irrotational fluid (initially at $y > 2$) inside the new mean shear flow (cf. figure 5*d*); this is clearly seen in the tracer concentration plots (figure 6*d*, *e*) where a band of concentrated fluid at the outer edge of the shear layer seals off an area of essentially zero-concentration fluid from the overlying zero-concentration area. (A similar kind of entrainment process was also proposed by Stern (1991) in a contour dynamics calculation of the interaction between a monopolar vortex and the edge of a variable-vorticity shear flow.) With increasing time (figures 3*e*, 4*e*, 5*e*, 6*e*) the dipoles retreat toward the wall until they encounter it, and in the case of the more-viscous run E2 the dipoles (figures 5*f*, 6*f*) become elongated in the new boundary layer, whereas the dipoles in E1 keep their identity longer until a second exchange of partners occurs

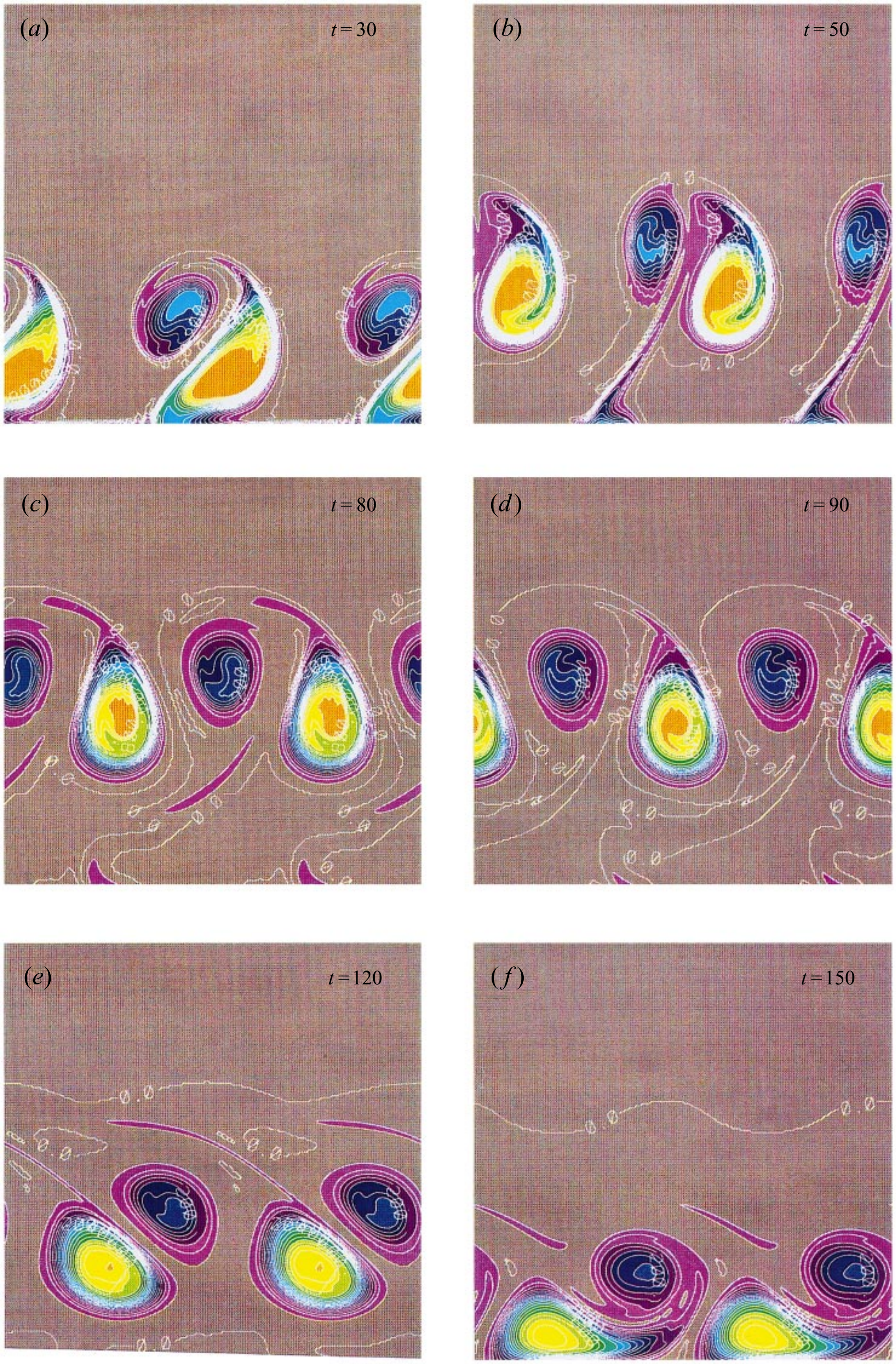

FIGURE 4(*a–f*). For caption see facing page.

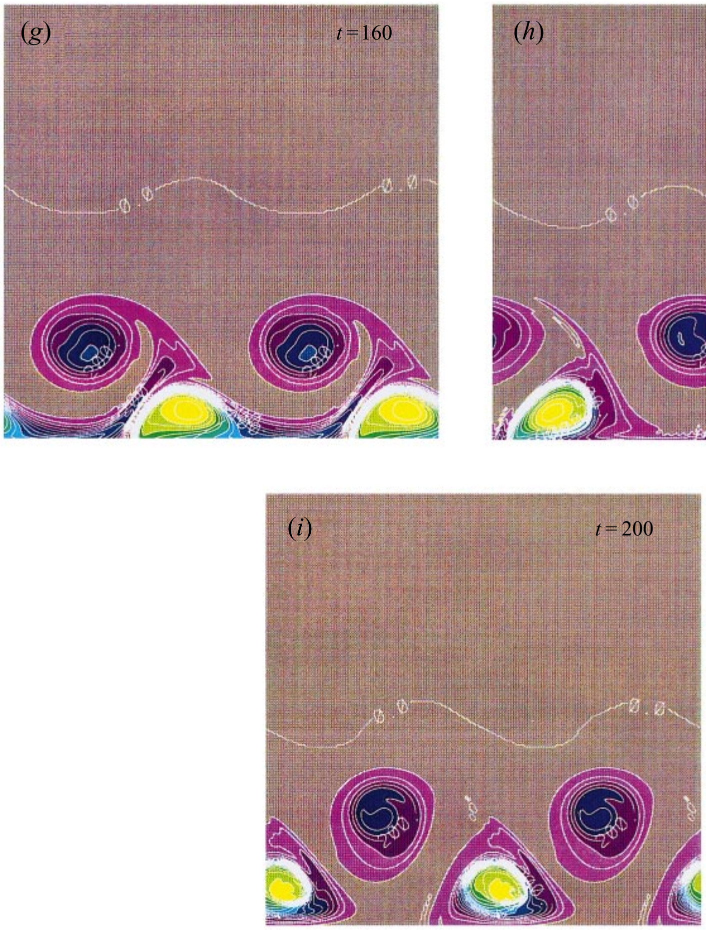

FIGURE 4. Tracer concentration fields for run E1 (free-slip boundary conditions, $A = 5 \times 10^{-4}$) at different representative times of the numerical integration. The contour interval is 50 and the colour code is given in the text. The diffusivity is an order of magnitude smaller than the viscosity.

(figures 3*f*, *g*, *h*, *i* and 4*f*, *g*, *h*, *i*), although not as far from the wall as in the previous exchange (figure 3*d*). A quite similar vorticity evolution occurs for the no-slip case E3 (figures 7, 8), and the completion of the entrainment process is again indicated by a band of concentrated fluid (figure 8*f*) at the outer edge of the shear layer.

Figure 9, for run E3 at $t = 70$, emphasizes the important kinematical difference between the monopolar velocity (or streamline) field in the unstable jet and the dipolar vorticity field. The predominant velocity structure consists of a periodic array of large eddies with an inner core of positive vorticity surrounded by an outer rim of negative vorticity, but with both regions circulating counterclockwise. Much smaller regions with closed clockwise streamlines lie between and below the big eddies. The dominant structures which are clearly visible in the dye pattern of the eddies in the laboratory experiment (figure 1*b*) correspond to the large eddies. This is this structure of combined positive/negative vorticity which will be modelled later on (§3.1) as a single eddy. An additional property of interest is the timewise evolution of the mean velocity field (figure 10), which shows that during the 'instability phase' ($t < 50$) there is an outward eddy diffusion of momentum, but in the subsequent 'entrainment phase' there is

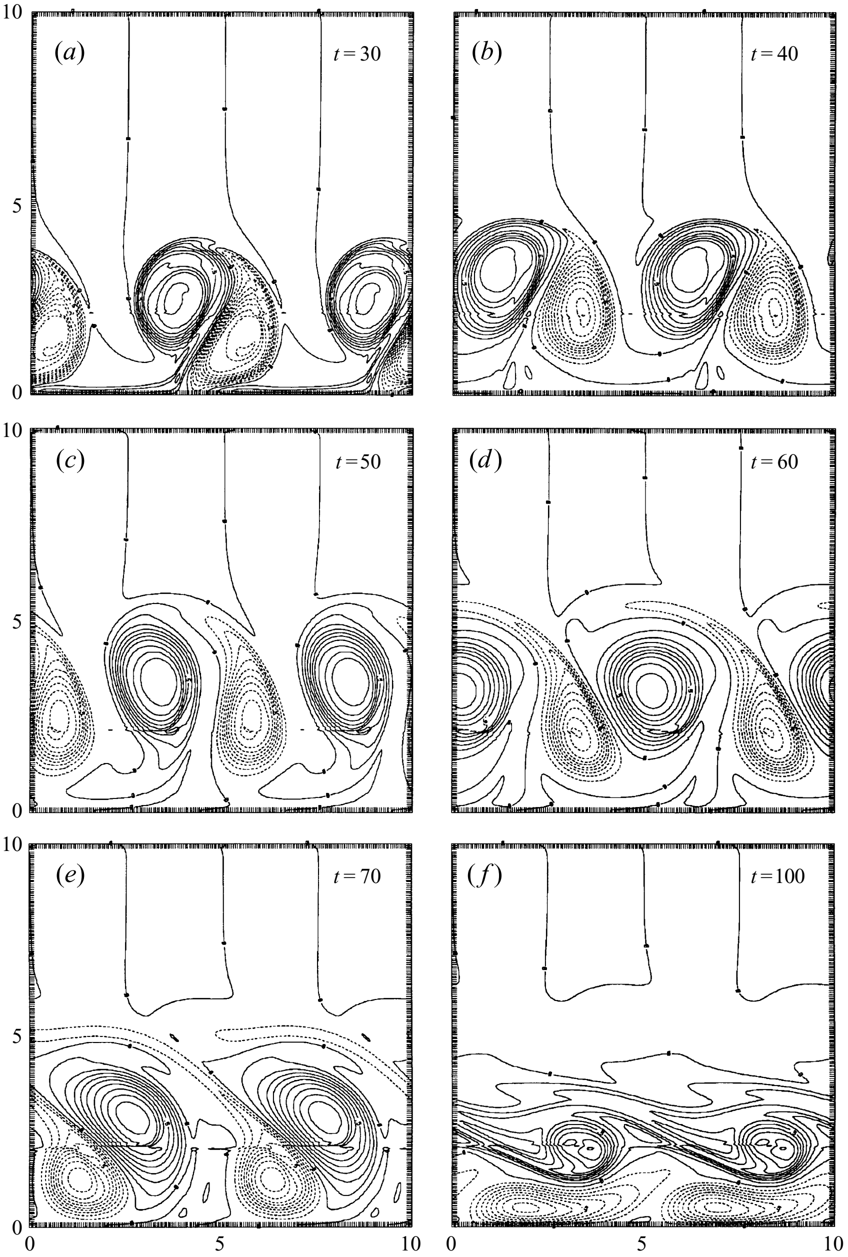

FIGURE 5. As figure 3 but for run E2 (free-slip boundary conditions, $A = 1 \times 10^{-3}$).

countergradient momentum flux which increases the maximum mean velocity as the eddy energy decreases. Also note that while $\bar{u}(0) = 0$ for the no-slip case, $\bar{u}(0) > 0$ is positive at $t = 50$) for free slip.

One major difference between free-slip and no-slip runs can be seen at $t = 50$ for E3 (figure 7*a*, just prior to the time when the vortices retreat to the wall) when compared to equivalent times for E1 and E2 (figures 3, 5): the thin layer of negative vorticity present near the wall in the no-slip case E3 is absent in the free-slip case (figures 3*b*, *c*, 5*b*). In both cases Stokes theorem requires the total spatially averaged vorticity to be

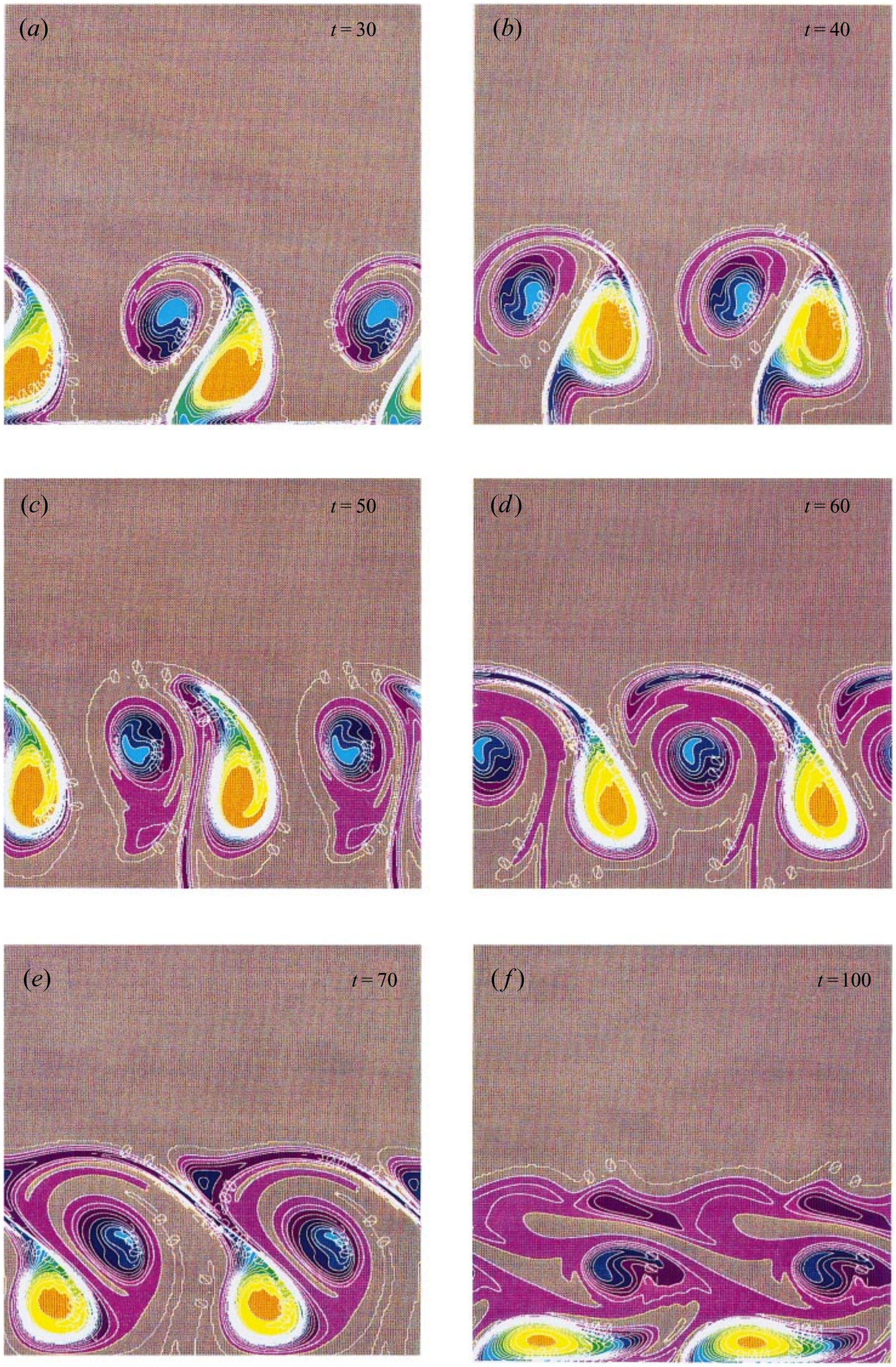

FIGURE 6. As figure 4 but for run E2 (free-slip boundary conditions, $A = 1 \times 10^{-3}$).

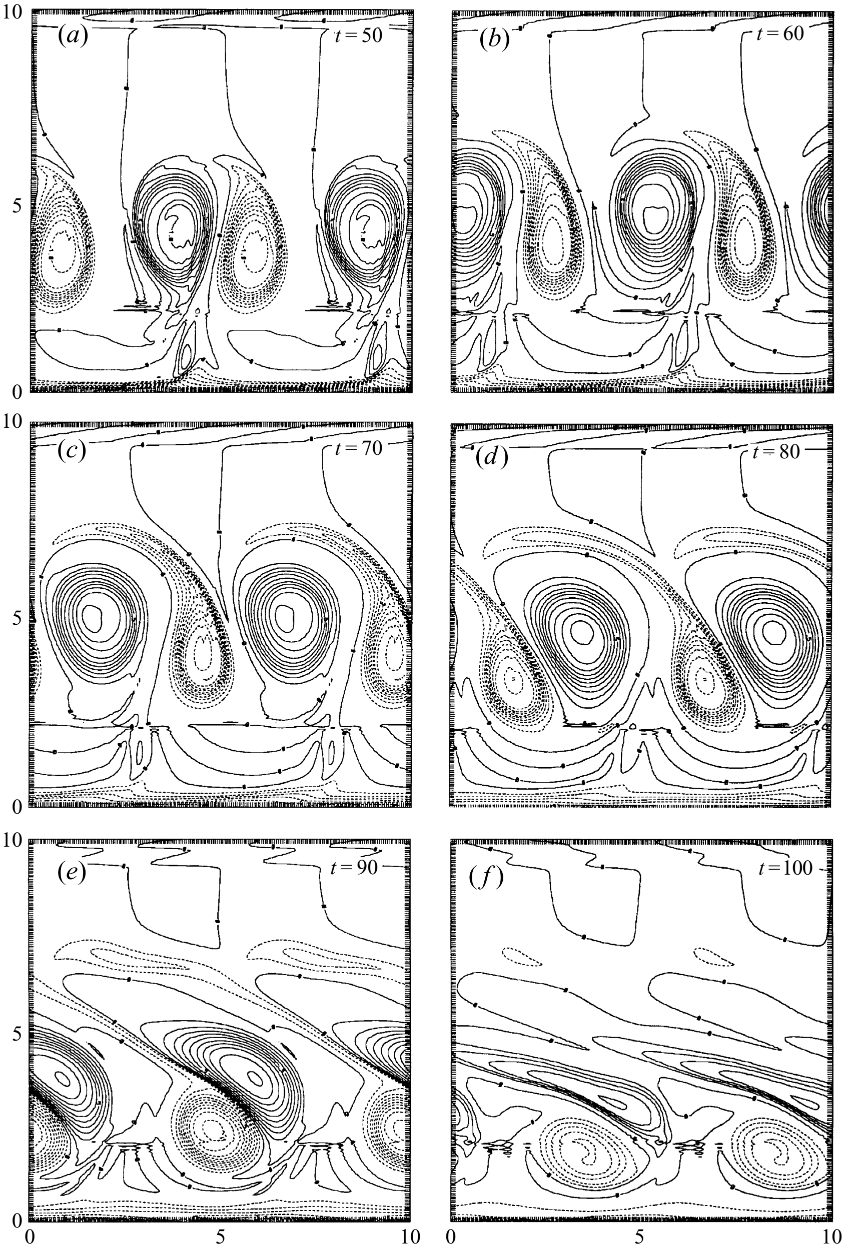

FIGURE 7. As figure 3 but for run E3 (no-slip boundary conditions, $A = 5 \times 10^{-4}$). This is the most important run. Note that the integrated negative vorticity in each dipole (far from the wall) is less than the integrated positive vorticity.

proportional to the average wall velocity $\bar{u}(0)$ and therefore this vorticity must vanish when the no-slip boundary condition applies. Therefore an excess of positive vorticity in the dipoles (figure 7*c*) is needed to compensate for the negative vorticity present in the thin layer near $y = 0$. The same excess of positive vorticity is required for the dipoles in the free-slip cases because (figure 10*a*, *b*) $\bar{u}(0) > 0$ and because the mean vorticity is zero on the wall. We emphasize this property of the eddy (excess positive

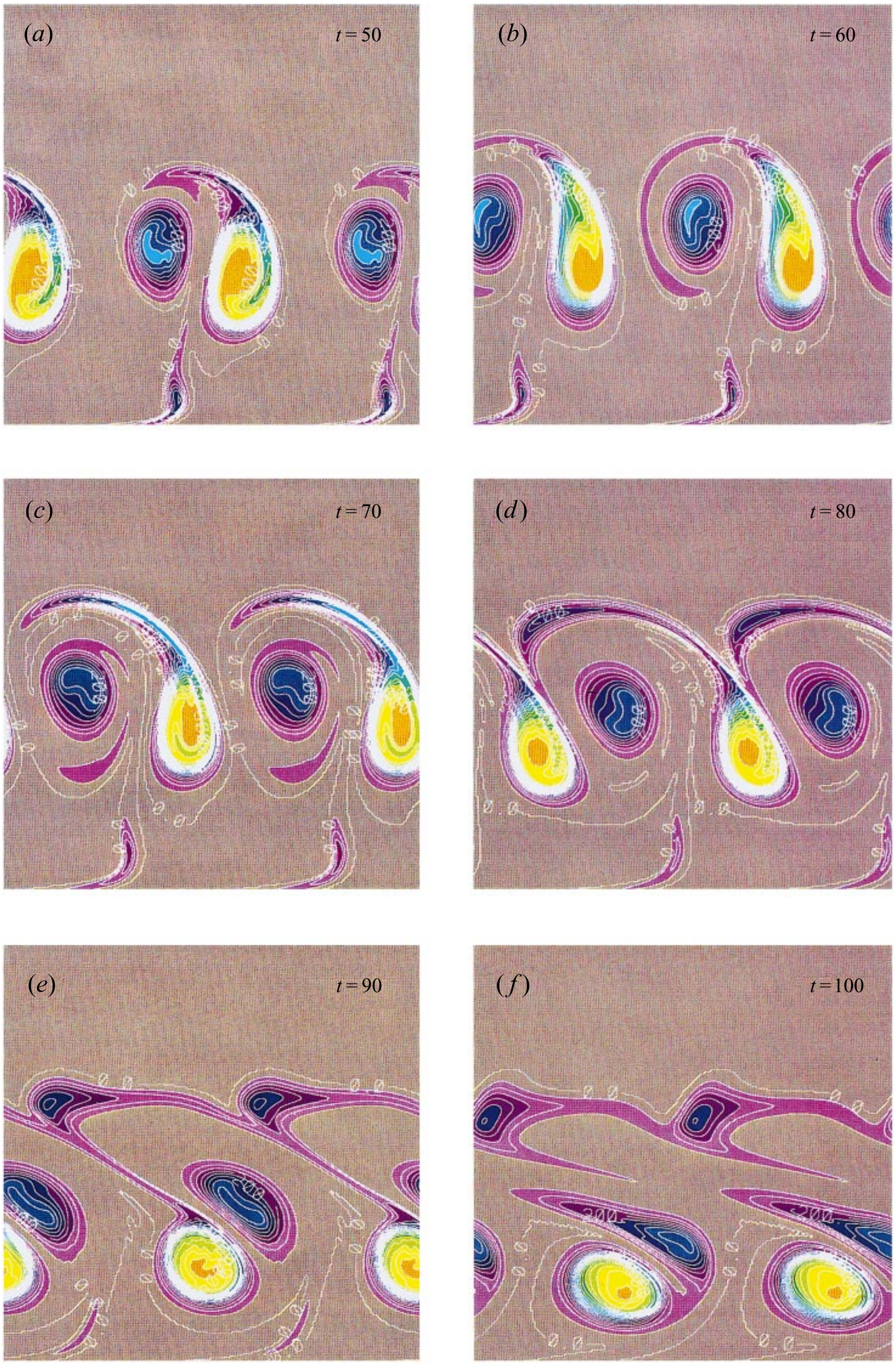

FIGURE 8. As figure 4 but for run E3 (no-slip boundary conditions, $A = 5 \times 10^{-4}$). This clearly shows that irrotational fluid initially outside ($y > 2$) the jet becomes irreversibly entrained inside.

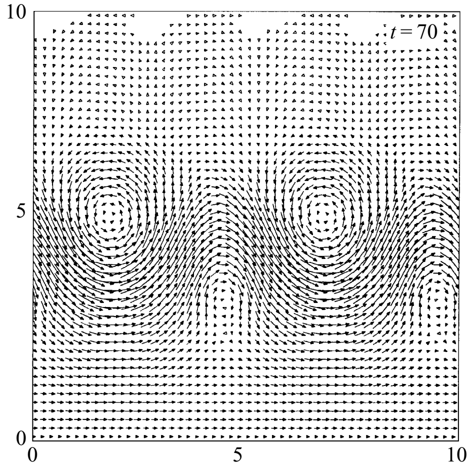

FIGURE 9. The total velocity vectors are plotted for E3 at $t = 70$ where the eddies are furthest from the wall. Note the monopolar character of this field, as compared with the concomitant dipolar vorticity field.

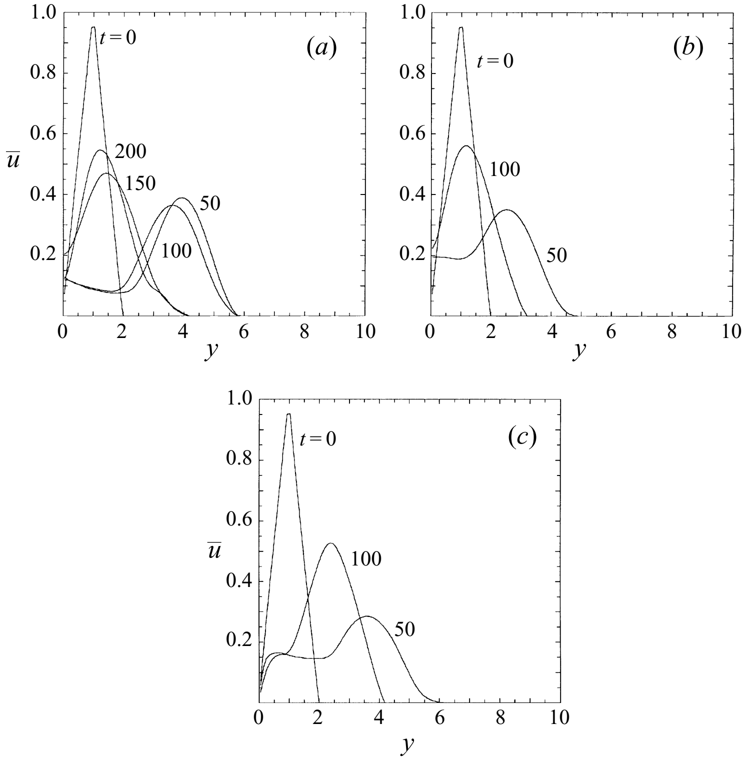

FIGURE 10. Cross-stream distribution of horizontally averaged downstream velocity at different times for (*a*) E1; (*b*) E2; (*c*) E3. Note that outward diffusion at small t is followed by inward retreat of the mean field.

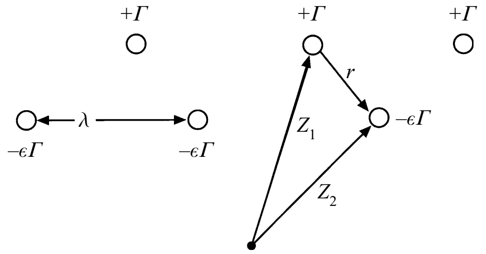

FIGURE 11. Point-vortex model explaining ‘exchange of partners’ (see §2.2). The complex separation distance $r = r_x + \mathrm{i}r_y$ has a component r_x in the horizontal direction, and r_y in the upward direction.

vorticity) at the end of the instability phase as it will be used in the subsequent consideration of the downstream evolution of a wall jet (e.g. figure 1*b*).

2.2. *A point-vortex model of the dipoles' evolution*

In order to emphasize the dynamical importance of the aforementioned vorticity imbalance, the evolution of the periodic array of dipolar eddies (cf. $t = 30$ in figure 3) with distributed vorticity is represented by a simple model consisting of a periodic array of co-linear point vortices of strength $\Gamma_1 = \Gamma > 0$ and separation λ, beneath which is another co-linear array of strength $\Gamma_2 = -\epsilon\Gamma$ and separation λ, where $0 < \epsilon < 1$. This inequality incorporates the main effect of the wall, namely that part $(1-\epsilon)$ of the negative vorticity which is left behind on the wall after the instability wave develops into the dipole. This effect may be attributed to the vanishing normal component of the velocity at the wall (in the inviscid case, figure 2), and/or to the vanishing of the tangential velocity at a non-slip wall (in the viscous numerical problem). In the present inviscid point-vortex model (figure 11), with the wall completely removed, our purpose is to see to what extent this simplification is able to explain the behaviour (e.g. exchange of partners) in §2.1. It is recognized that if the lower set of vortices is too near a wall, an entirely different and dynamically irrelevant behaviour would be obtained.

Let $Z_1(t)$ denote the complex vector position of any designated positive vortex in the periodic array, and $Z_2(t)$, the position of its nearest neighbour in the negative array at $t = 0$. The velocity field produced by each array at any field point is well known (Lamb 1945), and from this we get the following equations of motion for the two representative vortices:

$$\frac{\mathrm{d}\overline{Z_1}}{\mathrm{d}t} = \frac{\mathrm{i}\Gamma\epsilon}{2\lambda}\cot\frac{\pi(Z_1 - Z_2)}{\lambda}, \tag{1}$$

$$\frac{\mathrm{d}\overline{Z_2}}{\mathrm{d}t} = \frac{\mathrm{i}\Gamma}{2\lambda}\cot\frac{\pi(Z_1 - Z_2)}{\lambda}, \tag{2}$$

where the bar denotes the complex conjugate. From this it follows that $Z_1/\epsilon - Z_2$ is independent of time, and also

$$\frac{\mathrm{d}r}{\mathrm{d}t} = \frac{\mathrm{i}\Gamma(1-\epsilon)}{2\lambda}\cot\frac{\pi\bar{r}}{\lambda}, \tag{3}$$

where
$$r = Z_1 - Z_2 = r_x + \mathrm{i}r_y \tag{4}$$

is the separation between the vortices in question. Equation (3) implies that the motion of the weaker vortex $(-\epsilon\Gamma)$ relative to the stronger one is the same as that of a passive tracer particle placed at a distance r from a vortex of strength $(1-\epsilon)\Gamma$ (located at the origin $(0,0)$) in a single periodic array along the real axis. The Lagrangian path of such a particle is merely the streamline ψ of the velocity components of (1) and (2) as given in Lamb (1945), namely

$$\psi = \cosh\frac{2\pi r_y}{\lambda} - \cos\frac{2\pi r_x}{\lambda}. \tag{5}$$

All streamlines with $|\psi| > 2$, give single-valued r_y with $r_y(t) \neq 0$, for all $-\infty < r_x < \infty$; otherwise ($|\psi| < 2$) the streamline (and the parcel path) is a closed curve ('cat's eye') encircling the designated positive vortex Z_1 at all times. In the former case ($|\psi| > 2$), a negative vortex Z_2 is sufficiently far from the positive vortex Z_1 that it is not captured, but is carried continuously downstream on a sinuous path which always lies below the time-dependent path of the positive vortices. Any designated negative eddy will continually change partners (i.e. its nearest positive neighbour), and the transverse velocity of each array will oscillate in time, depending on whether the negative vortex is leading or lagging its present partner. This conclusion holds for all ϵ. From (1)–(4), it also follows that

$$\frac{\mathrm{d}}{\mathrm{d}t}\left(Z_1 - \frac{\epsilon r}{1-\epsilon}\right) = 0 \tag{6}$$

and therefore the horizontal (x) components of displacements are related by

$$x_1(t) - \frac{\epsilon}{1-\epsilon} r_x(t) = \text{constant}. \tag{7}$$

It is easy to see that the inequality $\psi > 2$ is satisfied for E1 (figure 3*b*) since $2\pi r_y/\lambda \sim 1.71$ [or $\cosh(2\pi r_y/\lambda) = 2.85$] and $2\pi r_x/\lambda \sim 2.35$ [or $\cos(2\pi r_x/\lambda) = -0.70$]. The same is true for E2 and E3 (figures 5*b* and 7*b*, respectively). To compare the results of (7) for the simple model with the numerical calculations (§2.1), the boundary of the positive (negative) eddy was taken to be at the 0.1 (-0.1) vorticity contour of E2 (figure 5). The numerically computed ratio Γ_2/Γ_1 of the integrated vorticities within these boundaries then gave an approximate value of ϵ at each time, and the centroids of these two areas provide the respective position vectors Z_1, Z_2; $r_x = x_2 - x_1$ is then plotted (figure 12) for run E2 as a function of x_1. Also listed are the corresponding values of ϵ, which have an average $\bar{\epsilon} = 0.7$. Nominal values of $\epsilon > 1$ occurred at the beginning and at the end of the run, but these correspond to dynamical stages not relevant near the time where dipole interaction leads to the exchange of partners, and consequently these points ($\epsilon > 1$) are not included. The remaining central points (with $\epsilon < 1$) have been bounded (figure 12) by two straight lines with essentially the same slope, and by using this in (7) we can predict an ϵ of 0.8. Since this is consistent with the average $\bar{\epsilon} = 0.7$ obtained from the numerical simulation (§2.1) the applicability of (7) is verified. The model (figure 11) is also able to qualitatively explain the variation in the ordinate of the centroid of the E2 vortices as given by the plot of $y_1(x_1)$ in figure 12. The important conclusion which will be used in §3 is that near the end of the instability phase the behaviour of the eddies in §2.1 can be explained by assuming each one contains a net positive vorticity ($\epsilon < 1$).

2.3. *The role of subharmonic instabilities*

In contrast to the separation of the jet in figure 1(*b*), the long-term evolution in the foregoing spatial instability is such that the current remains bound to the wall. The question then arises as to whether this will change when additional disturbances of larger horizontal scale are introduced. In the case of non-rotating free jets and shear

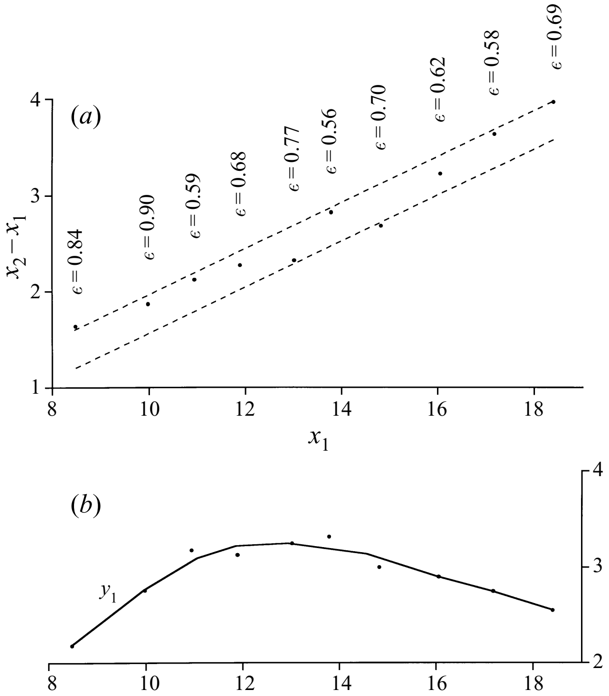

FIGURE 12. (*a*) The vortex centroid separation distances $x_2 - x_1$ for run E2 as a function of x_1 with the corresponding ϵ listed. The slope of the fitted straight lines are used with (7) to determine an independent value of ϵ, to test the ability of the point vortex model (figure 11) to explain the E2 run. (*b*) The y_1 variation. See text.

layers, the superposition of a subharmonic wavelength on the most unstable mode induces pairing of adjacent vortices, which results in a downstream increase of the width of the current (Saffman 1995). A similar qualitative behaviour is expected in our two-dimensional wall jet, and one may ask whether this effect will be indicative of the kind of separation observed in figure 1(*b*). The numerical simulation of §2.1 with no-slip boundary conditions and with $A = 5 \times 10^{-4}$ was therefore repeated by adding an initial disturbance with twice the x-wavelength and with the same amplitude as used in §2.1. In addition, the width of the computational domain was doubled in the y-direction in anticipation of an increase in the transverse spread of the current. The evolution of the vorticity plots at times prior to $t = 30$ (figure 13*a*) is similar to that which occurs in the absence of the subharmonic, except for a modulation produced by the longer wavelength, such that alternate dipoles appear further from the wall. While these dipoles continue their outward propagation, the inner dipoles reverse the slope of their axis ($t = 65$; figure 13*b*) and move back toward the wall; there is also an accumulation of negative vorticity on the wall as in the run without subharmonics (§2.1). Note that these inner dipoles are smaller than the outer ones, in which the positive vortex is especially large. The negative vortex in the outer dipole is in the process of being strained due to the opposing circulation of the adjacent positive vortices and this effect is clearly shown at $t = 90$ (figure 13*c*) where half of the outer negative vortex has been stripped away from its outer positive partner by the inner positive vortex. This removal of the outer negative vorticity, in addition to the changed inclination of the outer dipole axis, is indicative of the fact that the maximum outward extent of the current has been reached. In fact, the major coupling of the outer positive

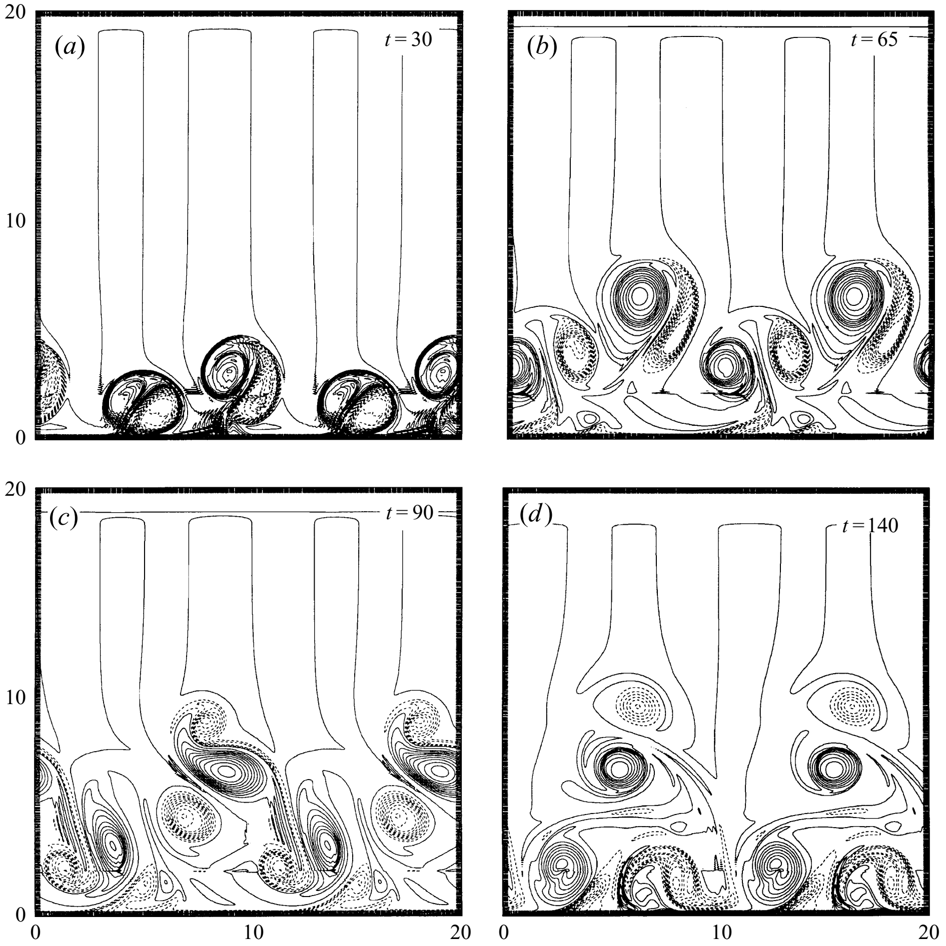

FIGURE 13. Vorticity fields for the subharmonic run (no-slip boundary conditions, $A = 5\times10^{-4}$) at different representative times of the numerical integration. The contour interval is 0.1. The fundamental wavelength ($\lambda = 4.87$) is the same as in figure 2.

vortex is not with the outer negative vortex, but with the nearest negative vortex on its opposite side; the interaction of these is such as to move the outer positive vortex back to the wall as appears at $t = 100$. As already mentioned, this is the signature of a counter-gradient momentum flux. As late as $t = 140$ (figure 13*d*), there is little indication of any further outward eddy diffusion. Although this complex process is clearly worthy of further investigation, relevant to the downstream increase in jet width, there is no indication that the subharmonic pairing process acting alone can produce a complete separation from the wall (figure 1*b*), and other processes must be considered.

3. The spatial evolution of a jet emerging from a source on the wall

The lack of periodicity in the spatial evolution of the wall jet poses a more complicated and difficult problem that the temporal evolution one discussed in §2. Some insight can be gained, however, by considering the full instability eddies as an

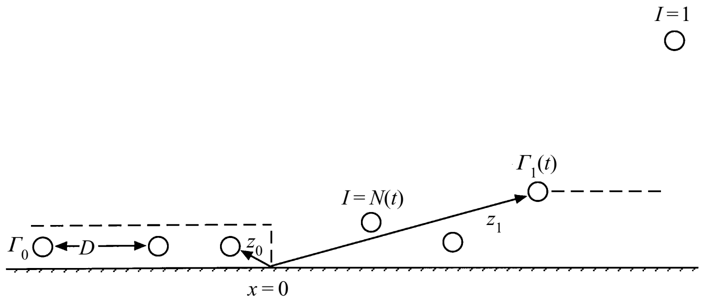

FIGURE 14. A heuristic model to explain the separation in figure 2. Point vortices (strength Γ_0) emerge from a 'nozzle' (the dashed-box at $x<0$). $Z_I(t)$ denotes the position of the Ith vortex after it emerges from the nozzle. See §3.1.

initial condition and by modelling them (§3.1) as point vortices periodically emitted from a source region on the wall. An emitted volume flux is also prescribed from this region which, combined with all the vortex interactions, carries the eddies downstream. From the major conclusion of §2 (see also discussion of figure 9 in §2.1), we assume that each of these periodically emitted vortices has a small net positive circulation, but no explicit dipolar vorticity structure. The statistical properties of the ensemble of slowly decaying vortices will provide the basis for the experimental investigation of the separation point in §3.2.

3.1. *A discrete-vortex interaction model*

The temporal evolution (§2) of periodic disturbances in the laminar wall jet contains important effects which are observed in the spatial evolution experiment (figure 1*b*), such as the fully developed eddies which propagate downstream. (Compare the tracer pattern in figure 8*a*, and the associated counterclockwise velocity structure (figure 9), with the dye pattern in figure 1*b*.) We may also assert (on the basis of §2.2) that each eddy in figure 9 has a small net positive circulation equal to the difference between the positive vorticity in the core and the negative vorticity which tends to be wound around the circumference of the eddy. However, the later stage of the periodic model (§2) in which the dipole members retreat toward the wall and exchange partners is not observed in figure 1(*b*), and the periodic model is also incapable of explaining the distance from the source region at which the eddies abruptly separate from the wall and gather in a large turbulent plume. A heuristic explanation of this will now be sought using a simple model which includes the following effects: (*a*) the mutual interaction between the wall eddies due to their aforementioned net positive circulation, (*b*) the advection of the eddies by the divergent mean flow emerging from the source region and (*c*) the downstream decrease of circulation in each eddy due to Ekman bottom friction. Any explicit effect of the distributed negative vorticity around the rim of each eddy will be neglected, as well as the lateral viscosity. Note that the Ekman boundary layer effect depends on the Coriolis parameter, and this is the only place where it appears parametrically in the two-dimensional theory.

The mathematical model illustrated in figure 14 consists of positive point vortices of strength Γ_0 periodically emitted at ($x=0$, $y=y_0$) from a source region ('nozzle') at $x<0$, and of a wall at $y=0$. Inside this (dashed-box) region there are 'controlled' point vortices which produce the external flow mentioned in (*b*), as well as supplying the 'active' vortices at ($x>0$) at equal time intervals. Suppose that at $t=0$, there is only a semi-infinite array of controlled vortices inside the box ($x \leqslant 0$) with constant strength

Γ_0, constant separation D, constant distance from the wall y_0, and moving with constant speed U_0 parallel to the wall. Suppose these values are controlled (by unspecified external forces) to have the same values at all subsequent times. When the leading Γ_0 vortex reaches the exit ($x = 0$) of the source region, it is no longer constrained but is free to move under the influence of the external ($x > 0$) flow field induced by all the vortices inside the source region, as well as by the field produced by all the free vortices previously emitted. Furthermore, suppose that the circulation $\Gamma(t)$ of each of the free vortices decreases at a rate s^{-1}, where s can be thought of as the Ekman 'spin-up' time. This parameterization is related to the theory of quasi-geostrophic eddies, in which case bottom friction causes relative vorticity to decay exponentially in a spin-up time which is inversely proportional to the square root of the Coriolis parameter.

If at time t, there are N such emitted vortices, with $Z_I(t) = x_I + \mathrm{i}y_I$ denoting the complex coordinate ($\mathrm{i} = (-1)^{1/2}$) of the $I < N$ member (and $\overline{Z_I}$ the complex conjugate), then

$$\frac{\mathrm{d}Z_I}{\mathrm{d}t} = \frac{\mathrm{i}}{2\pi}\sum_{\substack{J=1\\J\neq I}}^{N} \Gamma_J(\overline{Z_I}-\overline{Z_J})^{-1} - \frac{\mathrm{i}}{2\pi}\sum_{J=1}^{N} \Gamma_J(\overline{Z_I}-Z_J)^{-1}$$

$$+\frac{\Gamma_0}{\pi}\sum_{m=0}^{\infty} y_0(\overline{Z_I}-\overline{Z_0}+mD)^{-1}(\overline{Z_I}-Z_0+mD)^{-1}, \quad t_N < t < t_{N+1}, \tag{8}$$

$$Z_0(t) = -D + (t-t_N)\,U_0 + \mathrm{i}y_0, \tag{9}$$

$$\Gamma_J(t) = \Gamma_0 \exp\left(-(t-t_J)/s\right), \tag{10}$$

where t_J is the time of emission of the Jth vortex, and $Z_0(t)$ is the position of the leading vortex inside the box. The first term on the right-hand side of (8) is the velocity induced on I by all the other free vortices, the second term is the velocity induced by the images of all the free vortices, and the last term is due to the flux emerging from the source region as parameterized by the irrotational velocity produced by the semi-infinite array of controlled vortices.

The value of U_0 which we decided to use for the internal propagation of the controlled vortices in the source region was half of the uniform free velocity of a doubly infinite array of uniformly spaced vortices above a wall, and according to Lamb (1945) this is

$$U_0 = \frac{1}{2}\left(\frac{\Gamma_0}{2D}\frac{1+\mathrm{e}^{-4\pi y_0/D}}{1-\mathrm{e}^{-4\pi y_0/D}}\right). \tag{11}$$

For the results presented below, the equations were non-dimensionalized by taking $y_0 = 1$ (as the length unit) and $\Gamma_0 = 4$; calculations were made only for $D = 2$, so that the corresponding value of $U_0 = 0.50187$ determines the velocity scale. The initial condition was $Z_1(0) = \mathrm{i}$, $Z_0(0) = -2+\mathrm{i}$; and a new vortex is emitted every $D/U_0 \sim 4$ time units. For the final results given below, a second-order Runge–Kutta time step of 1/25 was used for $s = s_1 = 25$. The calculation extends over a time interval such that 100 vortices were emitted; for the less-viscous case in which $s = s_2 = 35$, 150 vortices were emitted. In each case the average centroid position

$$\langle x\rangle + \mathrm{i}\langle y\rangle = \frac{1}{N}\sum_{I=1}^{N} Z_I \tag{12}$$

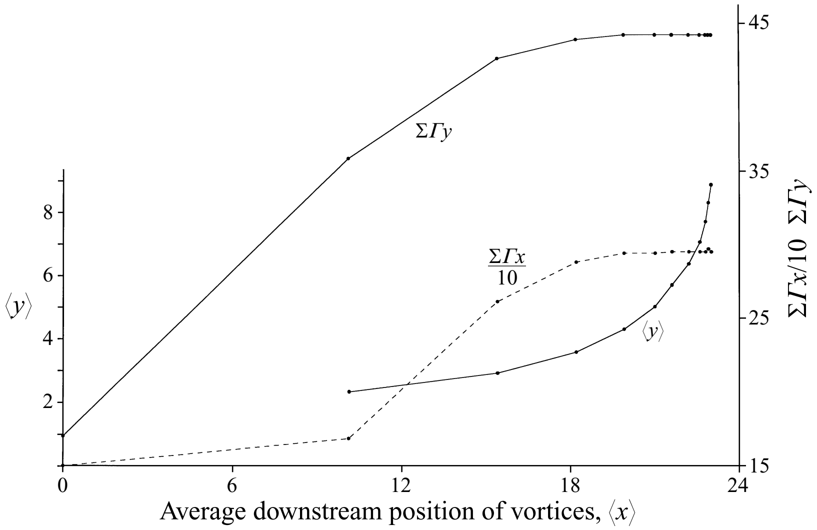

FIGURE 15. Statistics of the point-vortex model in figure 14. The average displacement from the wall ($\langle y\rangle$) is plotted as a function of average downstream distance $\langle x\rangle$ for $N(t)$ vortices. The circulation-weighted displacements (right hand scale) are also plotted at equal time increments of 40. $\Gamma_0 = 4$, $y_0 = 1$, $D = 2$, $s = 25 \equiv S_1$.

was computed as well as the circulation-weighted displacement

$$\sum_{I=1}^{N} \Gamma_I x_I + \mathrm{i} \sum_{I=1}^{N} \Gamma_I y_I = \sum_{I=1}^{N} \Gamma_I Z_I. \tag{13}$$

Note that the continuum limit of (13) is $\iint \mathrm{d}x\,\mathrm{d}y\,\zeta(x,y,t)\,(x+\mathrm{i}y)$. This first moment of the vorticity, (13), is dynamically more significant than the average centroid position (12), which gives undue weight to the large number of dissipated vortices at large times.

The computed centroid coordinates from (12) for $s = s_1 = 25$ are plotted in figure 15 at intervals of 40 time units, and are connected by straight lines. An approximate (or slowly varying) asymptote at abscissa $x_*(s_1) \simeq 23$ appears where $\langle y\rangle$ starts to increase rapidly. A scatterplot (not shown) of all 100 point vortices at this time ($t = 438.4$) revealed a line of 'young' vortices propagating rapidly along the wall to a distance from the nozzle approximately equal to this $x_*(s_1)$, at which point they move rapidly away from the wall and enter a broad elliptical region containing rather uniformly distributed vortices with a maximum $x = 43$ and a maximum $y = 19$. Since many of the latter are very 'old' ($\Gamma(t_I)) \rightarrow 0$ they merely constitute passive tracers whose individual positions are subject to significant numerical errors despite the small time step (1/25). The average displacement computed is however believed to be accurate to better than 10%. Of greater accuracy and dynamical significance are the circulation moments (13) plotted as a function of $\langle x\rangle$ in figure 15, where asymptotic values of (13) are clearly indicated at large time t. Qualitatively similar results for $s = s_2 = 35$ are indicated in figure 16. An extrapolation of the $\langle y\rangle$ curve suggests an approximate asymptote, corresponding to that in figure 15, of $x_*(s_2) \simeq 35$, and the ratio for the two runs is

$$\frac{x_*(s_2)}{x_*(s_1)} \simeq \frac{35}{25}.$$

The somewhat fortuitous agreement of this with s_2/s_1 suggests that the point vortices

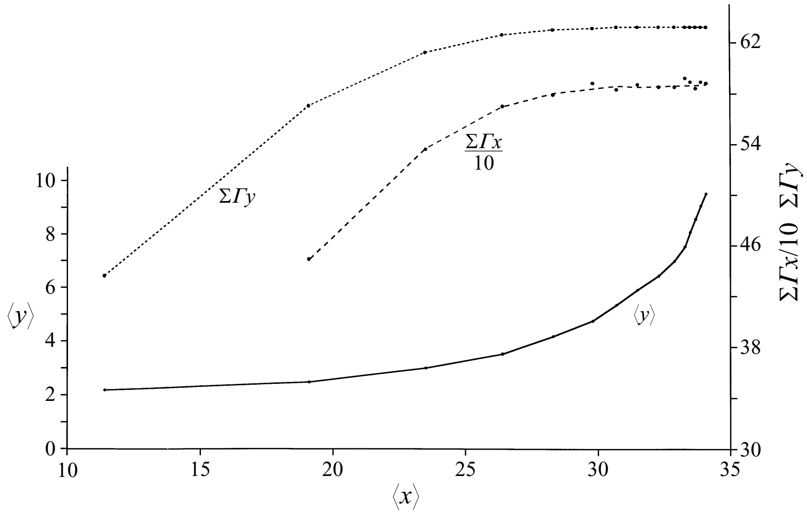

FIGURE 16. Same as figure 15 except the spin-up time is $s = 35 \equiv S_2$.

propagating along the wall will erupt into a plume at a downstream distance x_* which scales with the spin-up time multiplied by a scale velocity U_0, i.e.

$$x_*(s) \sim sU_0, \tag{14}$$

provided y_0 and Γ_0 are held constant. Figures 15 and 16 also show that for equal values of $\langle x \rangle$ (e.g. 23) the value of $\langle y \rangle$ for $s = 35$ is much less than the value for $s = 25$. In the latter case, the transverse displacement induced by (young) upstream vortices on (old) downstream ones is larger than for the $s = 35$ case. Although it is not surprising that the asymptotic $\sum \Gamma_I x_I = 590$ for $s_2 = 35$ is larger than the $\sum \Gamma_I x_I = 295$ for $s_1 = 25$, the ratio of the moments (590/295) is much larger than s_2/s_1, which suggests that these moments depend on the number N_* of vortices having significant strength at a given time. This N_* depends not only on the emission frequency (U_0/D), but also on their decay times, i.e. $N_* \sim sU_0/D$. Thus $\sum \Gamma_I x_I$ not only scales with $\Gamma_0(sU_*)$, for reasons previously given, but also with some unknown function of $N_* = sU_0/D$ which apparently increases rapidly with its argument. Since $y_0 = 1$ is the same for both runs, the larger value of $\sum \Gamma y$ for $s_2 = 35$ can also be attributed to the larger value of s_2.

Although we should not attempt any direct connection between figure 1(*b*) and this mathematical model, the result suggests a mechanism, testable as indicated in the following laboratory experiments, whereby young instability eddies catch up with older ones and gradually push them away from the wall.

3.2. *Laboratory experiments*

In a rapidly rotating fluid, the decay of eddies, or the 'spin-up time', is proportional to $H/(\nu f)^{1/2}$ where H is the depth of the layer, f is the Coriolis parameter, and ν is the molecular viscosity. Equation (14) suggests that an appropriately defined separation distance x_s of the wall jet should scale with the product of this spin-up time and a typical jet velocity, such as Q/LH, where Q is the volume discharge, and L is the transverse width of the current. This asymptotic scale distance may be rewritten as $x_s = d_s(H/L)$, where

$$d_s = Q/(H(\nu f)^{1/2}). \tag{15}$$

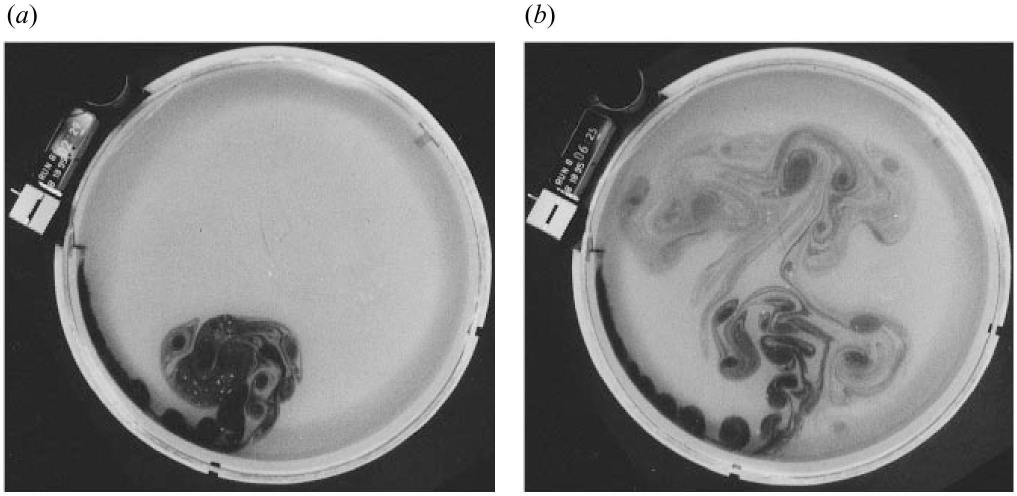

FIGURE 17. The present experiment for $f = 1.2\ \mathrm{s}^{-1}$, $Q = 12.0\ \mathrm{cm}^3\ \mathrm{s}^{-1}$ at two times ((*a*) $t = 2$ min 29 s and (*b*) 6 min 25 s), showing the fully developed instability eddies, their downstream propagation, the separation point x_s (the furthest downstream distance on the wall where dye appears), and the merger of eddies in a large plume extending normal to the wall.

Since an appropriate and unique experimental L is difficult to define or measure, we decided to look for a correlation between (15) and x_s, this being simply taken as the downstream position $x_s(t)$ of the leading edge of the dyed fluid on the circular wall.

The experimental set-up was similar to that used by Stern & Whitehead (1990), and the reader is referred to that paper for measurements of the mean velocity in the barotropic portion of the jet. The tank (figure 1*b*) diameter was 213 cm, the free surface height was 20 cm, and the jet was produced by the flow from three horizontal nozzles, which were 4.76 cm long and 0.14 cm in diameter. These were mounted above each other 5.0 cm apart, and directed parallel to the wall in the same sense as the rotation. Thermal uniformity (better than 0.1 °C) of the tank and source waters was assured before starting, and the top of the tank was covered by a frame-mounted cellophane wrapper, through which continuous video pictures could be taken by a distant overhead camera. The density change in the wall current induced by the neutral dye is $O(10^{-5})$ and makes a negligible baroclinic contribution to the current's strength. The three thin jets issued from the nozzles emerged 10 cm downstream, and at 20–30 cm downstream, the two-dimensional Taylor-column effect could be seen in the form of the instability waves and eddies. The nozzle orientation (as well as H) was kept constant in all of the following runs, each of which was begun by turning on the source pump after the tank rotation rate had been constant for at least eight spin-up times.

A non-rotating ($f = 0$) run indicated qualitative consistency of the mean velocity with that of the classical wall jet, and twenty runs were taken with various combinations of $f = 0.4$, 0.6, 0.8, 1.8, $1.2\ \mathrm{s}^{-1}$, and $Q = 3.2$, 3.7, 4.8, 6.3, 8.1, $16.3\ \mathrm{cm}^3\ \mathrm{s}^{-1}$. All of these produced dye patterns qualitatively similar to the earlier one (figure 1*b*) in which barotropic instability waves were seen to evolve into a series of round cyclonic eddies separated by entrained (clear) fluid. Each eddy propagated downstream with diminishing speed, eventually to be displaced normal to the wall, where it merged with an older eddy inside the large plume (figure 17). By sprinkling small paper pellets in the upstream wall jet, we could see that shortly before reaching the separation point virtually all of the current was deflected away from the wall with

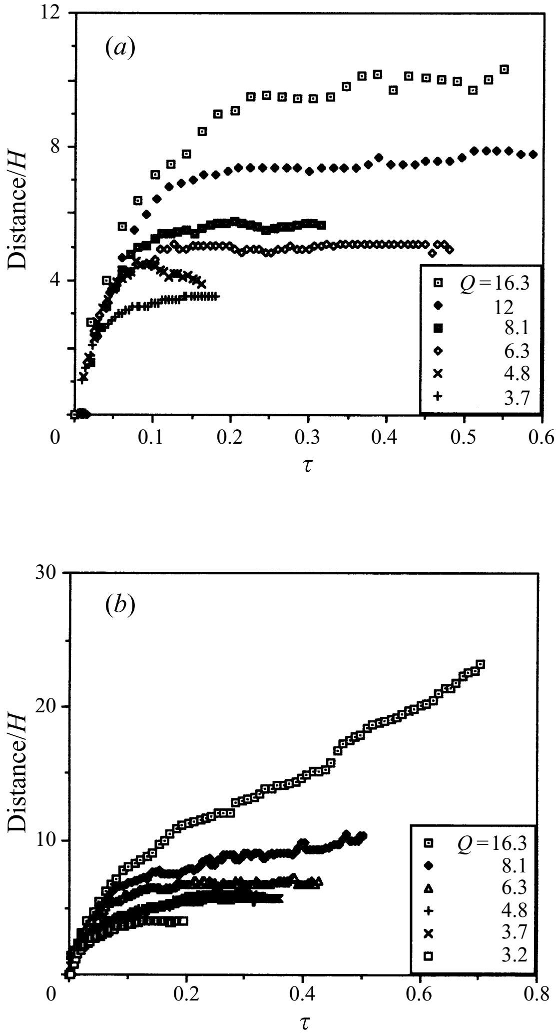

FIGURE 18(*a*,*b*). For caption see facing page.

a velocity comparable with the typical upstream value. The separation point x_s, on the other hand, drifted downstream at a much slower rate and in some cases came to a virtual halt. This occurs for all Q in the runs (figure 18*a*) with the highest rotation rate of $f = 1.2\ \mathrm{s}^{-1}$. An asymptotically constant $x_s(t)$ also occurs for $f = 0.8\ \mathrm{s}^{-1}$ (figure 18*b*) at the lower flow rates ($Q \leqslant 8.1\ \mathrm{cm}^3\ \mathrm{s}^{-1}$); and for $f = 0.6\ \mathrm{s}^{-1}$ (figure 18*c*) at $Q \leqslant 6.3\ \mathrm{cm}^3\ \mathrm{s}^{-1}$; and for $f = 0.4\ \mathrm{s}^{-1}$ at only the lowest flow rate of $Q = 3.7\ \mathrm{cm}^3\ \mathrm{s}^{-1}$. A steady asymptotic value for x_s was not reached for the other runs (those at large Q and at smaller f) in which the measurement was stopped because of the large displacements and because it seemed as if the separation point was going to continue to drift around the circumference. The experiments can also be characterized by the Rossby number $Ro = Q/fHL^2$. A typical estimate of the width L of the jet at the onset of the shear instability is of the order of 5 cm (see for example figure 1*b*) which produces a range in Rossby number from 0.006 to 0.08. It is found that a steady asymptotic value of x_s was reached for all runs with $Ro < 0.03$.

There was a clear and distinct structural difference in the plume between those runs

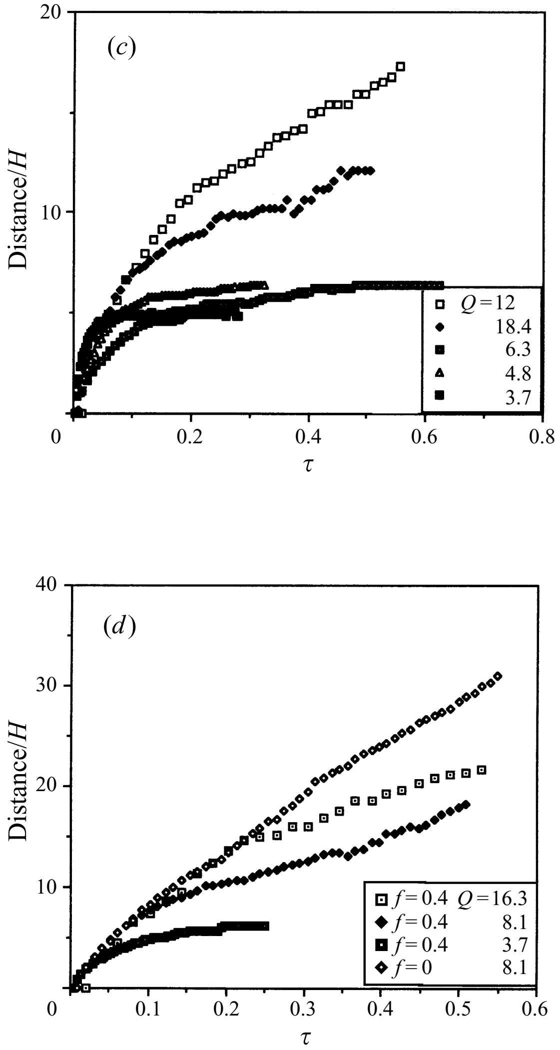

FIGURE 18. The ordinate is the non-dimensionalized downstream 'distance' of the leading edge of the dye on the wall (see figure 17) normalized by the depth, and the abscissa is time non-dimensionalized by (H^3/Q). (*a*) $f = 1.2$, (*b*) $f = 0.8$, (*c*) $f = 0.6$, (*d*) $f = 0.4$. Also included in (*d*) is the position of the nose of the dye pattern in the non-rotating case.

in which the separation point stopped and those in which it moved. Visual observations were conducted in three ways: watching the original experiment, viewing the tape in real time, and viewing the tape in fast forward. If the separation point stopped, some clockwise eddies coming off the wall paired with counterclockwise eddies offshore, and the large plume of dye moved offshore in a direction roughly normal to the wall. One could see both counterclockwise and clockwise circulation patterns offshore, and regions of assorted sizes would pair up into counterclockwise and clockwise pairs that had a net offshore movement.

In contrast, if the separation point continued to drift slowly along the wall, fewer clockwise eddies were visible as partners to the counterclockwise eddies that moved offshore. The entire plume tended to be more circular and formed a gyre with an overall counterclockwise circulation. Those clockwise eddies seen offshore were

4. Conclusions

The first part of this paper (§2) concerns the long-time evolution of a normal-mode disturbance in a two-dimensional wall jet at large Reynolds number. It is shown that the well-known dipolar eddy appearing at the end of the linear growth phase does not continue propagating away from the wall because the integrated positive vorticity in the dipole exceeds the negative vorticity, and because the interaction of all the elements in the periodic (rectilinear) array causes the negative-vorticity patches to propagate downstream faster than the positive ones. The resulting change in nearest neighbour causes an entire eddy to reverse its outward displacement and to move back towards the wall. This phase was successfully explained in §2.2 by a simple model consisting of two arrays of point vortices with unequal strength, and located relatively far from the wall. At later times the more detailed numerical calculations (§2.1) also reveal a counter-gradient momentum flux involving an increase of mean field energy, a decrease in eddy kinetic energy, and a completion of the entrainment process (figure 8) in which irrotational fluid is irreversibly incorporated inside the new mean vorticity field formed by the instability.

The second part of this paper is concerned with the mechanism producing the separation from the wall of the two-dimensional jet emerging from a source region; this involves the somewhat different problem of spatial evolution. Nevertheless, the foregoing temporal instability process is relevant up to the time of maximum displacement of the dipolar eddy from the wall (figure 9). In this figure we note that each of the periodic eddies consists of a counterclockwise-circulating velocity field, with the clockwise vorticity located on the outer rim. Since the point-vortex model (§2.2) is able to explain the dynamics of this phase, we used such a model to elucidate aspects of the separation mechanism observed in figure 1(*b*). The mathematical model defined in §3.1 consists of monopolar point vortices representing the net positive circulation of the eddy (figure 9) with no explicit negative vorticity. These vortices are periodically emitted from a nozzle along with an irrotational mass flux. A crucial additional ingredient is that the strength of each emitted vortex decreases at a rate inversely proportional to the spin-up time, the latter being related to the effect of Ekman friction on a real eddy. The numerically computed statistics of a large number of emitted vortices suggest that the average distance from the source at which the vortices separate from the wall is proportional to sU_0, equation (14).

The last part of this paper tests this idea by means of a laboratory experiment in which the spin-up time is varied by changing the Coriolis parameter f, for various volume flux rates (Q) emerging from nozzles placed on the nearly straight vertical wall of a tank. It was found (figure 19) that for appropriately large f and small Q, the downstream position x_s of the wall separation point (as determined from the leading edge of the dye (figure 17)) increases with the scale distance d_s (15), which is the decay time $H(2f)^{-1/2}$ times the velocity Q/H^2. This supports the conclusion that bottom friction is important for the spectacular separation (figure 17) of the two-dimensional wall current.

It should be mentioned that f could be parametrically important for the two-dimensional flow in another sense, besides the Ekman layer. The dynamically significant width L of the wall jet which evolves (~ 20 cm) downstream from the nozzles depends (in a complex way) on f as well as on the three-dimensional turbulence; it would be worthwhile to eliminate this effect by using smoother inlet conditions. We plan to include the effect of the Ekman layer in numerical calculations of the spacewise evolution of a jet flowing from a source into a region of open boundary conditions.

We thank John Salzig for help with the laboratory apparatus and the photography. Partial support for the laboratory study was by the Coastal, Arctic and Physical Oceanography sections of the Office of Naval Research under contract N00014-89-J-10237. Melvin Stern was supported by the National Science Foundation through Grant OCE9529261. Eric Chassignet was supported by the National Science Foundation through Grant OCE9406663. Most of this work was performed at the Geophysical Fluid Dynamics Summer Study Program held at WHOI in 1995.

REFERENCES

Bidlot, J. R. & Stern, M. E. 1994 Maintenance of continental boundary shear through countegradient vorticity flux in a barotropic model. *J. Fluid Mech.* **271**, 55–85.

Bleck, R & Boudra, D. B. 1986 Wind-driven spin up in eddy-resolving ocean models formulated in isopycnic and isobaric coordinates. *J. Geophys. Res.* **91**, 7611–1621.

Boris, J. P. & Book, D. L. 1973 Flux-corrected transport. A fluid transport algorithm that works. *J. Comput. Phys.* **11**, 38–69.

Etling, D., Hansen, R. & Jürrens, R. 1993 The development of mushroom-like vortices in shear flow instabilities. *Dyn. Atmos. Oceans* **20**, 107–126.

Haidvogel, D. B., McWilliams, J. C. & Gent, P. R. 1992 Boundary current separation in a quasigeostrophic, eddy-resolving ocean circulation model. *J. Phys Oceanogr.* **22**, 882–902.

Lamb, H. 1945 *Hydrodynamics*, 6th Edn. Dover.

Saffman, P. G. 1995 *Vortex Dynamics*. Cambridge University Press.

Stern, M E. 1991 Entrainment of an eddy at the edge of a jet. *J. Fluid Mech.* **228**, 343–360.

Stern, M. E. & Whitehead, J. A. 1990 Separation of a boundary jet in a rotating fluid. *J. Fluid Mech.* **217**, 41–69.

Wygnanski, I., Katz, Y. & Horev, E. 1992 On the validity of various scaling laws to the turbulent wall jet. *J. Fluid Mech.* **234**, 669–690.

Zalesak, S. T. 1979 Fully multidimensional flux-corrected transport algorithms for fluids. *J. Comput. Phys.* **31**, 335–362.